On the wurtzite to tetragonal phase transformation in ZnO nanowires

On the wurtzite to tetragonal phase transformation in ZnO nanowires

Jun Wang[1], Yaogen Shen[2], Fan Song[1], Fujiu Ke[3], Xiaozhou Liao[4] and Chunsheng Lu[5]

[1] State Key Laboratory of Nonlinear Mechanics (LNM), Institute of Mechanics, Chinese Academy of Sciences, Beijing 100190, People's Republic of China
[2] Department of Mechanical and Biomedical Engineering, City University of Hong Kong, Kowloon, Hong Kong, People's Republic of China
[3] School of Physics and Nuclear Energy Engineering, Beihang University, Beijing 100191, People's Republic of China
[4] School of Aerospace, Mechanical and Mechatronic Engineering, University of Sydney, Sydney, NSW 2006, Australia
[5] Department of Mechanical Engineering, Curtin University, Perth, WA 6845, Australia

E-mail: wangjun@lnm.imech.ac.cn

CrossMark

Abstract

There is a long standing contradiction on the tensile response of zinc oxide nanowires between theoretical prediction and experimental observations. Although it is proposed that there is a ductile behavior dominated by phase transformation, only an elastic deformation and brittle fracture was witnessed in experiments. Using molecular dynamics simulations, we clarified that, as the lateral dimension of zinc oxide nanowires increases to a critical value, an unambiguous ductile-to-brittle transition occurs. The critical value increases with decreasing the strain rate. Factors including planar defects and surface contamination induce brittle fracture prior to the initiation of phase transformation. These findings are consistent with previous atomistic standpoints and experimental results.

Keywords: ZnO nanowires, phase transformation, size effect, strain rate, molecular dynamics

(Some figures may appear in colour only in the online journal)

1. Introduction

Nanostructured zinc oxide (ZnO) compounds are attractive materials due to their exceptional optical, electrical and mechanical properties. For these reasons, they are used in a wide range of applications including energy and environment [1–4], biomedical devices [5], nanoelectronics [6] and mechanical damping technology [7]. These applications mainly benefit from the unique surface feature of materials at the nanoscale where a large surface-to-volume ratio with a magnitude of 10^6–10^9 m^{-1} breaks an atomic symmetry on the surface of nanostructured ZnO [8, 9]. Theoretical analysis based on molecular dynamics (MD) simulations have shown that there is noticeable surface stress, which increases Young's modulus of ZnO nanobelts as their lateral dimensions are reduced [10]. The finding was verified by subsequent experiments on ZnO nanowires (NWs) [11, 12]. The

large surface-to-volume ratio also brings an atomic mobility with higher energy in ZnO nanostructures in contrast to their bulk counterparts. Thus, ZnO nanostructures are highly active to reconstruct under external stimulation. Phase transformation is such a reconstruction initiated by mechanical loading. The mechanically initiated hexagonal [13] and tetragonal [14] phases in ZnO NWs can lead to continuous interests since similar transformations are prevalent in a large variety of II–VI, III–V and IV–IV wurtzite structured ceramics [15–18].

With the ability of phase transformation, nanoscale ceramics have two distinct advantages. First, phase transformation improves their deformability. Taking the wurtzite to tetragonal phase transformation in ZnO NWs as an example, the initial wurtzite structured NWs yields 6.5%–10.0% strain at the elastic limit [19, 20]. These values fall at the middle of experimentally measured fracture strain, 2%–15%, of wurtzite structured ZnO NWs [19, 21–23]. After phase transformation,

fracture strain reaches to 17%–20% [19, 20]. Most importantly, unloading of transformed NWs leaves 6%–7% residual strain, declaring a phase transformation dominated ductility [24]. Second, there is a reversible transition from wurtzite to tetragonal reconstruction that was observed on the {01$\bar{1}$0} surface of ZnO nano-islands via *in situ* transmission electron microscopy [25]. This indicates that ZnO nanostructures have potential applications in shape memory devices [26].

Although the reversible wurtzite to tetragonal phase transformation offers ZnO nanostructures promising shape memory applications and the tetragonal phase has been experimentally witnessed [25, 27], there exists a puzzle between theoretical prediction and experimental observations. The tetragonal phase was firstly captured by MD in simulating the tensile deformation of ZnO NWs [14]. However, so far only brittle fracture of wurtzite structured ZnO NWs was observed in tensile experiments [12, 19]. To resolve this conflict, a theoretical study was recently conducted based on MD simulations using the reactive force field and *ab initio* calculations. It was found that the wurtzite to tetragonal phase transformation significantly depends on the lateral dimension of ZnO NWs, strain rate and temperature [20]. Although the lateral dimension was up to 4.8 nm in simulations, it is still much smaller than the lowest dimension (∼20 nm) experimentally tested [12, 28]. Moreover, it is argued that the transformation was forbidden under temperatures below 600 K [20]. This view is against that of a previous large-scale density functional theory analysis, which shows that the transformation occurred at 0 K [29].

It is seen that the tensile response of ZnO NWs is still illusive with two unsolved problems. One is the necessary requirement permitting the wurtzite to tetragonal phase transformation. The other is a reasonable interpretation of the large dispersion in fracture strain, 2%–15%, of wurtzite structured NWs [19, 21–23]. Motivated by these two contradictions, we performed systematic MD simulations on the tensile deformation of ZnO NWs in this paper. In section 2, the simulation techniques are introduced. Section 3 is then dedicated to a detailed description of tensile deformation of ZnO NWs with and without phase transformations. Factors that facilitate and hinder the phase transformation are discussed in section 4. Finally, some concluding remarks are given in section 5.

2. Simulation procedures

2.1. Microstructures in ZnO NWs

In ZnO NWs, three low-indexed growth directions, [0001], [2$\bar{1}\bar{1}$0] and [2$\bar{1}\bar{1}$3], have been identified [30]. These NWs exhibit triangle, rectangle and hexagonal cross-sections. Here we focus on [0001]-oriented NWs with the hexagonal lateral shape because a tetragonal phase has been detected on these NWs and sufficient experimental data and theoretical data are available for comparison [12, 14, 19, 20]. Moreover, intrinsic point and planar defects as well as extrinsic factors such as surface contamination are prevalent in ZnO NWs

Table 1. Parameters of the interaction potentials for ZnO in equations (1) and (2) [33].

Atom pair	Type	A (eV)	ρ (Å)	C (Å^{-1})
Zn–Zn	Born–Mayer	78.91	0.5177	
Zn–O	Born–Mayer	257600	0.1396	
O–O	Morse	0.1567	3.4050	1.164

[7, 31, 32]. These factors can have undeniable impact on tensile behaviors of NWs. It has been confirmed that point defects cause the scatter of fracture strain of wurtzite structured NWs [21]. However, to the best of our knowledge, the role of planar defects and surface contamination in tension of ZnO NWs remains unexplored. Therefore, these two microstructures are also taken into account.

2.2. MD simulation

The interatomic interactions in ZnO are described by an *ab initio* based pair potential. Specifically, the non-coulombic interactions V of short-range Zn–O and Zn–Zn are expressed by the Born–Mayer model, that is

$$V(r_{ij}) = A\mathrm{e}^{-r_{ij}/\rho}, \tag{1}$$

where r_{ij} is the distance between atoms i and j, and A and ρ are parameters mainly related to the hardness and size of ionic species [33]. Moreover, a Morse-type potential,

$$V(r_{ij}) = A[(1 - \mathrm{e}^{-C(r_{ij}-\rho)})^2 - 1], \tag{2}$$

is employed to represent the short-range O–O interaction, where C is a fitting parameter and its value is listed in table 1 [33]. The long-range Coulombic interactions are considered by assigning cations and anions to an effective charge of ± 1.14 e (here e is the unit of electronic charge).

As is known, surface contamination can stem from carbon during tensile tests in the chamber of a scanning electron microscope [12]. Platinum can also cause contamination when ZnO NWs are welded to the testing system by electron beam induced deposition [12]. Moreover, fabricating NWs by focused ion beam may introduce gallium ions [34]. Thus, it is reasonable to consider these effects as a realistic surface contamination scenario. However, to the best of our knowledge, there is still lack of such an interatomic potential between any of these three elements and ZnO. In this work, to evaluate the effect of surface contamination on the tensile behavior of ZnO NWs, we resort to a recently developed Rahman–Stillinger–Lemberg potential that models the interaction between silver (Ag) and particles in ZnO, that is

$$V(r_{ij}) = D\mathrm{e}^{y\left(1 - \frac{r_{ij}}{r_0}\right)} + \sum_{k=1}^{3} \frac{a_k}{1 + \mathrm{e}^{b_k(r_{ij}-c_k)}}, \tag{3}$$

where the related values of parameters D, y, r_0, a_k, b_k and c_k are listed in table 2 [35].

The motion of atoms was integrated using a Verlet leapfrog algorithm with a time step of 1 fs. The long-range Coulombic interactions were calculated by the Wolf sum [36]. To obtain free-standing configurations, samples were relaxed

Table 2. Potential parameters for interaction between Ag and ZnO in equation (3) [35]. The units of D and a_k ($k = 1, 2, 3$) are eV; r_0 and c_k are Å; b_k is Å^{-1}; and y is dimensionless.

Atom pair	Potential parameters		
Ag–Zn	$D = 185.4810$	$r_0 = 1$	$y_1 = 4.2084$
	$a_1 = -0.0231$	$b_1 = 5.2619$	$c_1 = 3.5369$
	$a_2 = -0.3764$	$b_2 = 1.8000$	$c_2 = 3.3262$
	$a_3 = 0.0038$	$b_3 = 0.9656$	$c_3 = 0.6894$
Ag–O	$D = 136.2424$	$r_0 = 1$	$y_1 = 5.0865$
	$a_1 = -1.5273$	$b_1 = 2.6489$	$c_1 = 2.1128$
	$a_2 = 1.8830$	$b_2 = 2.6256$	$c_2 = 1.6708$
	$a_3 = -0.3976$	$b_3 = 1.0508$	$c_3 = 0.4472$
Ag–Ag	$D = 206.4544$	$r_0 = 1$	$y_1 = 1.6171$
	$a_1 = -75.7945$	$b_1 = 2.2129$	$c_1 = 1.6720$
	$a_2 = -17.0348$	$b_2 = 1.4495$	$c_2 = 2.2826$
	$a_3 = -0.5642$	$b_3 = 0.6884$	$c_3 = 0.0914$

for 200 ps before stretching. To simulate tension and obtain the mechanical properties of ZnO NWs, an extra velocity was applied along the [0001] orientation at each integral step via a modified isothermal–isobaric ensemble [10, 37, 38]. This scheme stretched NWs with strain rates ranging from 2.5×10^9 to $0.25 \, \text{s}^{-1}$. The stress tensor was calculated by the classical virial formula and the system temperature was controlled by the Nosé–Hoover thermostat [39, 40]. All simulations were carried out by using a modified version of the DL_POLY package [38].

2.3. Selection of the interatomic potential

It is known that the accuracy and credibility of simulating results depend significantly on the interatomic potential employed. To choose a proper one, we have checked four types of potentials developed based on diverse physical models: a self-consistent potential with a Morse function [41], a Buckingham potential adopted a core–shell model [42], the reactive potential aiming to explore structures and reaction dynamics such as bond breaking and formation [43] and a new *ab initio* based potential for accurate simulation of phase transformation in ZnO [33]. The self-consistent one failed to predict the wurtzite to tetragonal phase transformation. The Buckingham type was non-reactive regarding to bond breaking and formation [20]. The reactive potential was also abandoned since it deviates from the prediction of the density functional theory at 0 K. Finally, the *ab initio* based potential was chosen because it performs well on the following four aspects: (i) the lattice constants of wurtzite and tetragonal phases it generated are consistent with that of the density functional theory [14, 33]; (ii) the thermal properties reconstructed echo with the experimental results and thus the temperature effect on phase transformation is detectable [33, 44]; (iii) surface energy was also modeled and this allows investigation on the size-dependent mechanical properties of ZnO NWs [33]; and (iv) most importantly, phonon dispersion calculated converges to the experimental data [33, 45]. This feature offers precision to study the strain rate effect on

deformation behaviors of NWs since the strain rate has much to do with the motion of phonons [46, 47].

3. Simulation results

3.1. Wurtzite to tetragonal phase transformation

A free standing ZnO NW adopts the wurtzite structure (i.e., the $P6_3mc$ space group) as shown in figure 1(a), which was generated by the visual MD software [48]. After phase transformation, the space group changes to $P4_2/mnm$. The transformed phase was previously referred to as the body-centered-tetragonal phase with four-atom rings, a term that has been widely applied to many II–VI, III–V and IV–IV compounds [14–18, 24]. Strictly speaking, however, since the four-atom ring at the center of a tetragonal lattice is perpendicular to those at the corners (see figure 1(a)), it is more precise to name the transformed phase as the tetragonal structure. The wurtzite to tetragonal transformation causes a three-stage stress–strain relation as a ZnO NW is uniaxially stretched. Figure 1(b) shows that the first stage from point A to point B is the elastic stretching process of the original wurtzite structure. Then, a sudden stress drop from point B to point C corresponds to a structural transformation. Finally, the transformed tetragonal structure is subjected to an elastic stretching from point C to point D before brittle fracture. Figure 1(c) illustrates that the stress drop initiated at point B is due to the breaking of Zn–O bonds along the [0001] orientation. However, no fracture occurs due to formation of an equal number of Zn–O bonds along the same direction next to the broken bonds. Breaking and formation of Zn–O bonds repeat on alternate planes along the [01$\bar{1}$0] direction that transforms the original wurtzite NW to a tetragonal one [24].

3.2. Size effect

To focus on the size-dependent tensile behavior of ZnO NWs, a strain rate of $2.5 \times 10^9 \, \text{s}^{-1}$ was chosen and temperature was maintained at 300 K. To compare with available results, we started from a NW with a lateral dimension of 1.0 nm. Figure 2(a) shows that the phase transformation initiates at the elastic limit with a strain of 8.0% and completes at the strain of 8.3%. These values are consistent with those predicted by the Buckingham potential [14, 19]. As the lateral dimension increases to 4.2 nm, the critical strain to trigger phase transformation rebounds to 10.2% and the transformation finishes at 11.0% strain. This agrees with that obtained by the reactive force field [20]. However, this differs from an investigation using the Buckingham potential. The corresponding strains were 6.5% and 8.0%, respectively, to trigger and complete phase transformation for a NW with a lateral dimension of 5 nm [19]. Taking bond rotation, bond breaking and bond formation into account, this difference is ascribed to failure of the Buckingham potential to capture the reactive feature in phase transformation [19]. Moreover, the previous investigation reveals that a transformed NW has a residual strain of 7% and maintains the tetragonal phase after unloading,
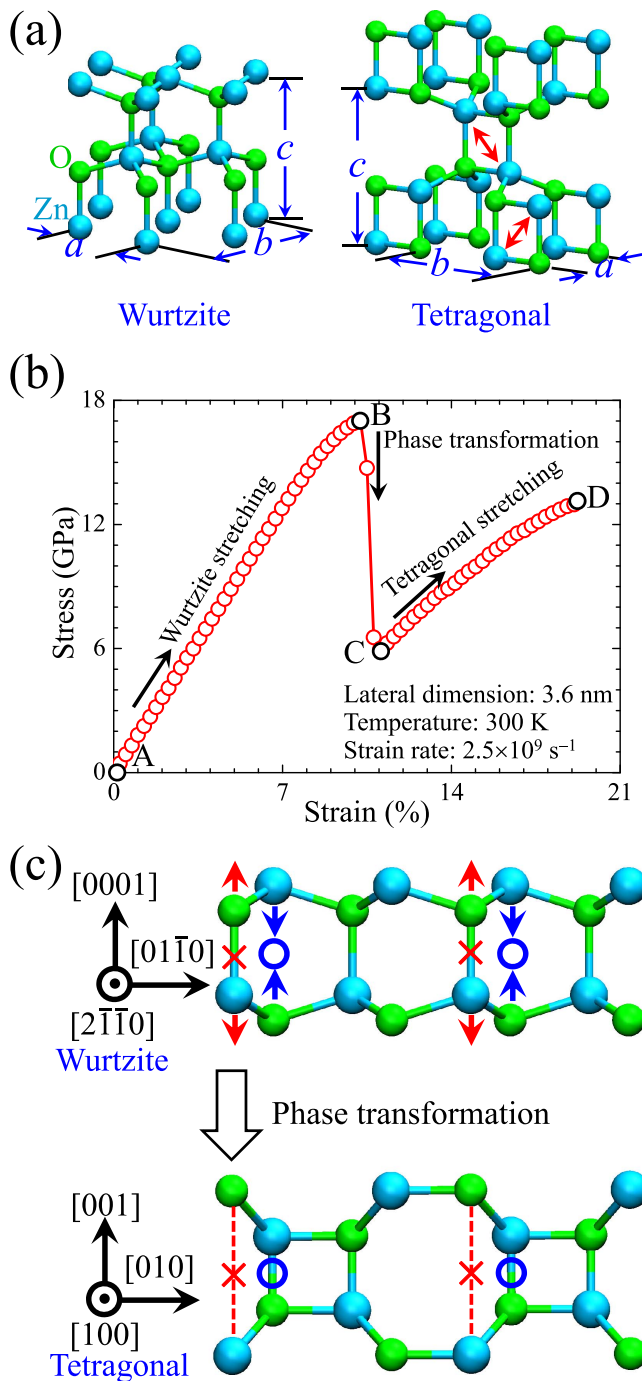
Figure 1. A sketch of the wurtzite-to-tetragonal phase transformation. (a) Wurtzite and tetragonal lattices. Two-way arrows point out mutually vertical orientations of four-atom rings located at the center and a corner of the tetragonal cell. (b) A typical stress–strain curve of ZnO NW with tension along the [0001] orientation. (c) The path of phase transformation from wurtzite to tetragonal structure. Arrows show relative motion of atoms. Crosses (×) and circles (○) mark positions where Zn–O bonds break and form, respectively.

Figure 2. Size-dependent tensile behavior of ZnO NWs. (a) Stress–strain curves of ZnO NWs with various lateral dimensions. (b) Strain at the elastic limit of wurtzite structure and strain at brittle fracture with various lateral dimensions of NWs.

transformation is detected. This does not contradict with previous simulations where a sample with a lateral dimension of 5 nm showed phase transformation. The reason for this seeming contradiction is due to the fact that the NW underwent quasi-static deformation without considering the effect of strain rates [19].

Critical strains at the elastic limit of wurtzite and fracture altering with the lateral dimension of NWs are summarized in figure 2(b). It is shown that strain at the elastic limit of wurtzite gradually increases from 8.0% to 10.2% as the lateral dimension increases from 1.0 to 3.6 nm. Then, the strain remains almost unchanged with the increase of lateral dimensions. Furthermore, fracture strain of ZnO NWs increases from 14.4% to 20% as the lateral dimension increases from 1.0 to 4.2 nm. However, it dramatically reduces to 10.2% with the lateral dimension beyond 4.9 nm due to elimination of phase transformation.

3.3. Strain rate

To describe the strain rate effect on tension of ZnO NWs, a NW with a lateral dimension of 10.1 nm and an aspect ratio of 2:1 was employed. The simulation temperature was

indicating a ductile behavior dominated by phase transformation [14, 24]. Here, it is worth noting that, however, an essential transition on the tensile behavior of ZnO NWs occurs as the lateral dimension exceeds 4.9 nm. In this case, brittle fracture occurs as the wurtzite structured NW reaches its elastic limit with a strain of 10.2% and no phase
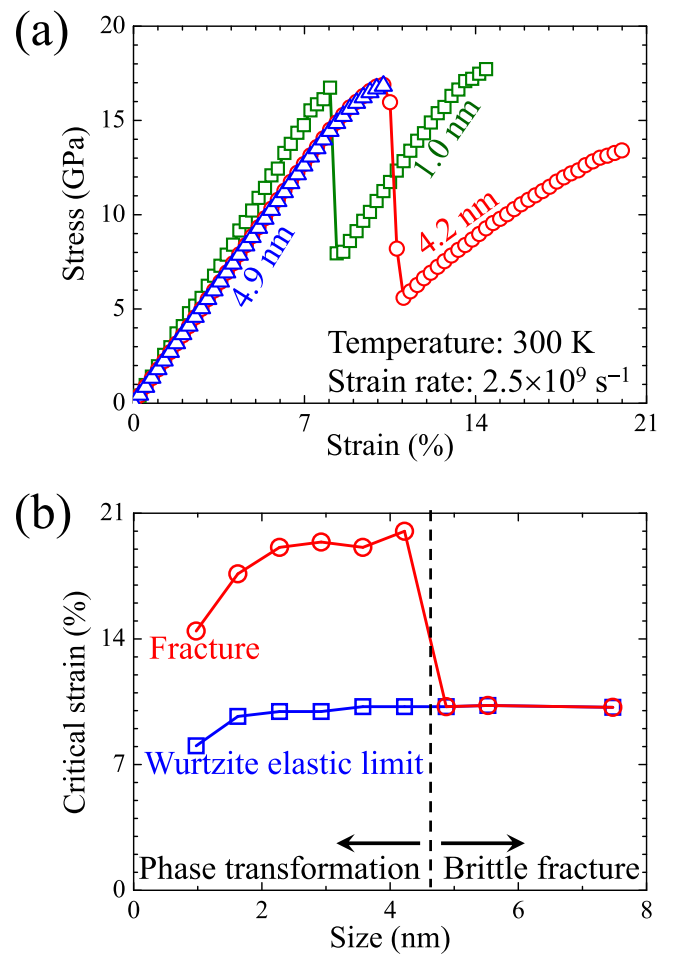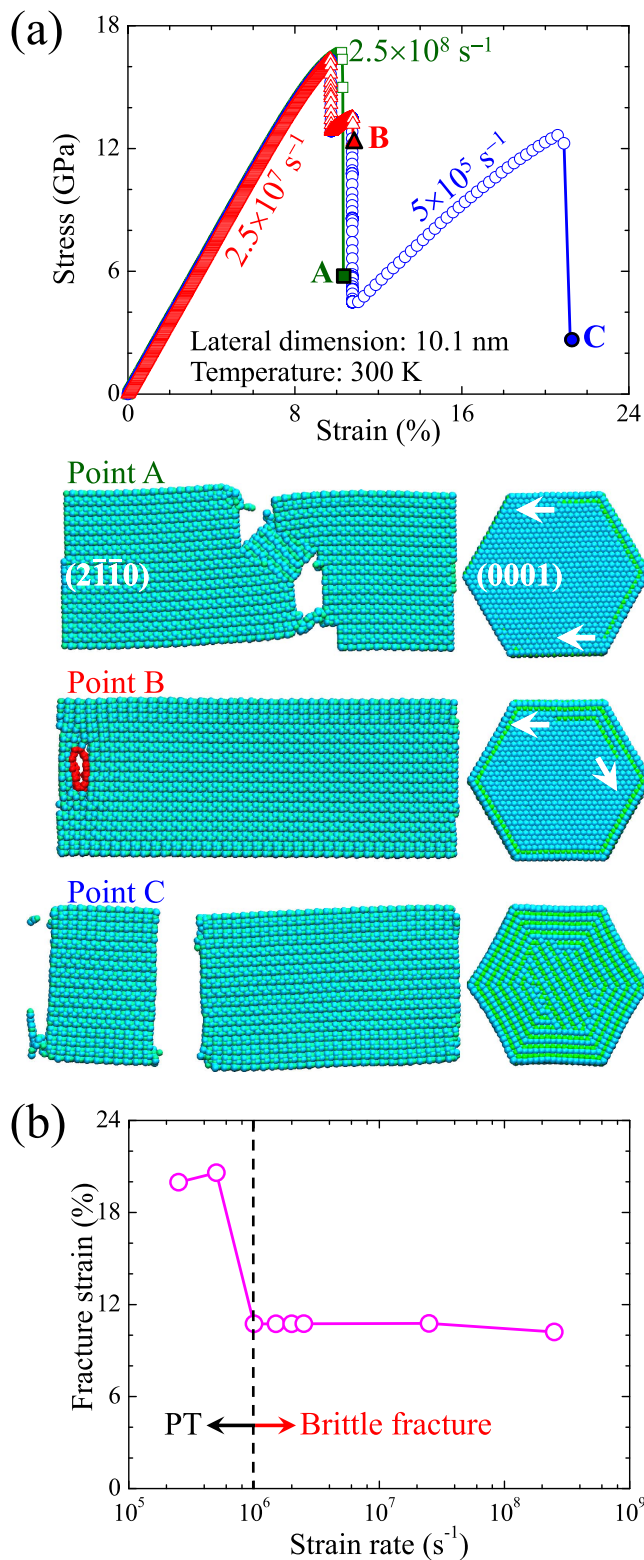
Figure 3. Effect of strain rate on tensile response of ZnO NWs. (a) Typical stress–strain curves with diverse strain rates. Arrows in snapshots represent spreading directions of tetragonal phase. Red atoms outline a crack. (b) Fracture strain varies with strain rate. PT indicates phase transformation.

maintained at 300 K. As shown in figure 3(a), at a strain rate of $2.5 \times 10^8\,s^{-1}$, the NW undergoes elastic stretching and the snapshot at point A reveals that phase transformation initiates at one ridge and propagates on its surface. However, propagation suddenly stops as soon as the NW exceeds its elastic limit and brittle fracture takes place. As the strain rate decreases to $2.5 \times 10^7\,s^{-1}$, the outmost surface layer of the NW completes transformation and the tetragonal phase starts to grow towards the NW core. Noticeably, the new phase still originates from the ridge side and spreads parallel to the NW surface until a crack perpendicular to the NW axis is generated at the intersection between wurtzite and tetragonal regions (see the snapshot at point B in figure 3(a)). The crack expands rapidly and causes brittle fracture, declaring the termination of phase transformation. To ensure transformation of the entire NW, the strain rate has to be reduced to below $5 \times 10^5\,s^{-1}$, as shown by the snapshot at point C in figure 3(a). It is seen that fracture strain (20.6%) of the transformed NW is at least 2 times of that (10.2%) of the original wurtzite one.

Fracture strain of the NW versus strain rate is drawn in figure 3(b). The tensile response of the NW shows three kinds of attributes with the reduction of strain rates: (i) as the strain rate is beyond $2.5 \times 10^7\,s^{-1}$, brittle fracture of wurtzite structure dominates tensile deformation of the NW; (ii) with further decrease of strain rates, incomplete phase transformation takes over at the range between 2.5×10^7 and $1 \times 10^6\,s^{-1}$; and (iii) the completion of phase transformation is allowed with strain rates below $5 \times 10^5\,s^{-1}$.

It is seen in table 3, the critical strain rate to initiate the wurtzite to tetragonal transformation reduces almost 10 orders of magnitude from 1×10^9 to $5 \times 10^{-1}\,s^{-1}$ as the lateral dimension of NWs increases from 4.9 to 19.8 nm.

3.4. Temperature effect

To ascertain the temperature effect on transformation, a NW with a lateral dimension of 5.5 nm and an aspect ratio of 2:1 was examined. The applied strain rate was $2.5 \times 10^9\,s^{-1}$ and simulation temperature was from 300 to 600 K. Figure 4(a) shows that as temperature is below 450 K, only elastic deformation and brittle fracture of wurtzite structured NWs are observed. However, with temperature over this critical value, stress–strain curves represent the three-stage attribution, indicating occurrence and completion of phase transformation. Critical strains at various temperatures are presented in figure 4(b). It is seen that, due to thermal softening, strain at the elastic limit of the wurtzite structure decreases with the increase of temperature. This result is consistent with previous studies [24]. Most importantly, it is shown that 450 K is the critical temperature for the wurtzite to tetragonal phase transformation.

3.5. Stacking faults

The wurtzite structure is one of the close-packed crystals with a periodic ABAB... stacking sequence. Here, A and B represent two of the three basic tetrahedral stacking units (i.e.,
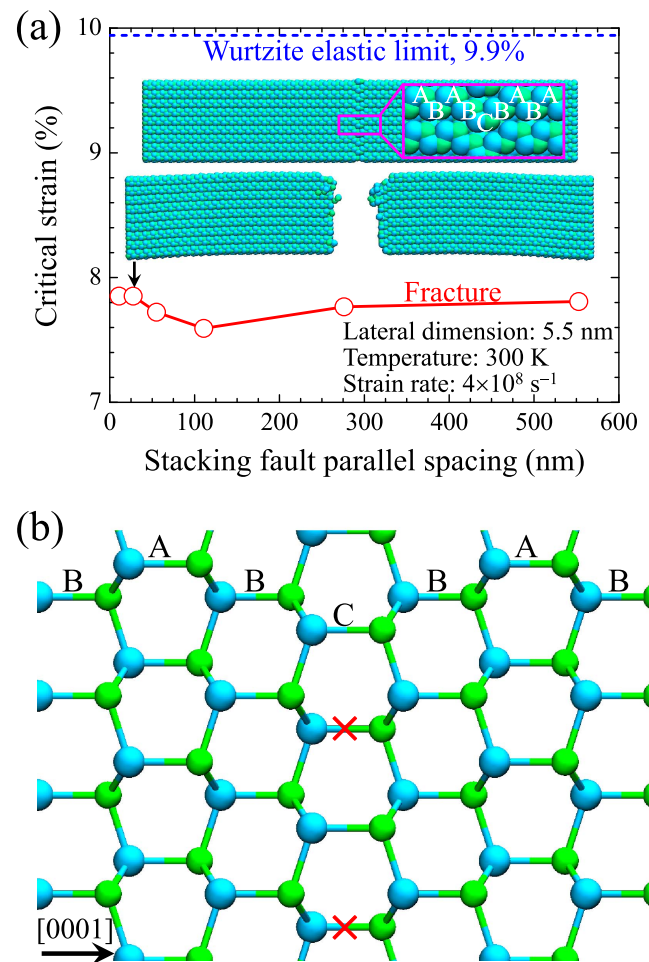
Table 3. Critical strain rates to initiate phase transformation with various lateral dimensions of NWs at 300 K.

Strain rate (s^{-1})	2.5×10^9	1×10^9	4.5×10^8	1.2×10^8	5×10^5	5×10^{-1}
Lateral dimension (nm)	4.2	4.9	5.5	7.5	10.1	19.8
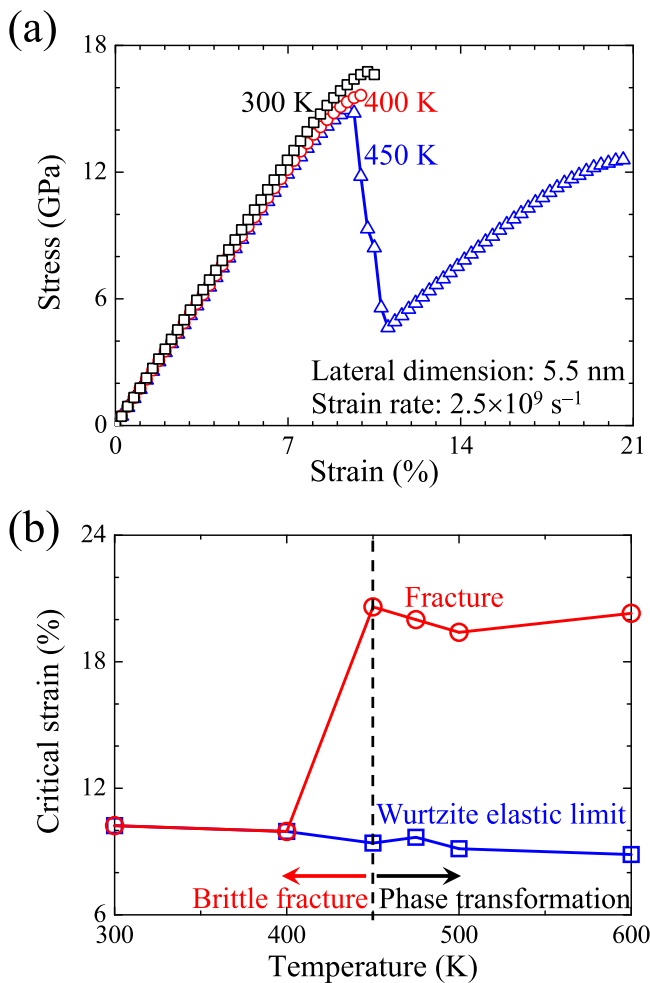
Figure 4. Temperature dependent deformation of ZnO NWs. (a) Stress–strain curves and (b) critical strains under several temperatures.

Figure 5. Stacking faults induce brittle fracture of wurtzite NWs. (a) Fracture strain of ZnO NWs with parallel spaced stacking faults. Insets show patterns of a NW with a parallel spacing of 27.6 nm between neighboring stacking faults before and after fracture. (b) Cracks initiate at sites marked by crosses (×) within a stacking fault.

A, B and C) [49]. Inserting C into the ABAB… sequence generates a stacking fault, see insets in figure 5(a). To investigate the effect of stacking faults on tensile deformation of ZnO NWs, a lateral dimension of 5.5 nm was considered. A strain rate of 4×10^8 s^{-1} was adopted and it is adequate to induce wurtzite to tetragonal transformation for a single crystal NW with the same lateral dimension at 300 K. A stacking fault was introduced at the middle of a NW and the periodic boundary condition was used along the axis. In such a design, spacing between parallel-spaced stacking faults is from 10.9 to 552.8 nm and aspect ratios of NWs vary from 2:1 to 100:1. Results show that spacing has negligible impact on fracture strain, which is around 7.7% ranging from 7.6% to 7.9%, see figure 5(a). Additionally, all samples maintained the original wurtzite structure until brittle fracture.

Figure 5(b) shows that Zn and O atoms at breaking Zn–O bonds (sites marked by crosses) in a stacking fault fail to reform along the [0001] orientation due to interruption of the wurtzite stacking regulation. As a result, cracks initiate at the breaking bonds and subsequently cause brittle fracture at the stacking fault.

3.6. Surface contamination

Contamination was considered by stochastically attaching Ag atoms on the surface of ZnO NWs. Ag atoms was introduced based on a concentration from 0.7 to 20 at%. NWs involved had a lateral dimension of 5.5 nm and an aspect ratio of 2:1. Tensile deformation was conducted with a strain rate of 4×10^8 s^{-1} at 300 K. These conditions ensure phase transformation of single crystalline wurtzite NWs with the same size. Results shown in figure 6 suggest that surface contamination hinders the wurtzite to tetragonal phase
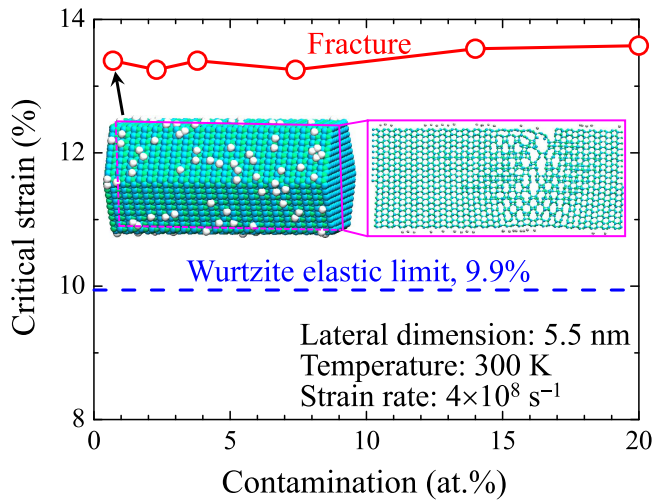
Figure 6. Fracture strain of ZnO NWs contaminated with Ag. Insets are original and fractured patterns of a NW with 0.7 at% surface contamination.

transformation. All samples are subjected to brittle fracture and the original wurtzite structure is maintained. However, it is of interest to note that even slight contamination could cause a substantial enhance of fracture strain. Taking the concentration of 0.7 at% for example, in comparison with that of the wurtzite structure, fracture strain was enhanced from 9.9% to 13.4%. Although Ag is not a realistic surface contaminant, the enhanced value is close to 12%–15% measured from experiments [22], where carbon, platinum and gallium ions were the most likely contaminants [12, 34].

4. Discussion

4.1. Wurtzite to tetragonal phase transformation

It is shown that wurtzite to tetragonal phase transformation in ZnO NWs is significantly size, strain rate and temperature dependent. To reveal the underlying mechanisms, we resort to the Arrhenius equation, that is

$$\dot{\varepsilon}_t = Be^{-E_a/k_B T}, \qquad (4)$$

where $\dot{\varepsilon}_t$ is the critical strain rate to trigger transformation, B is the pre-exponential factor, E_a is the activation energy for the wurtzite to tetragonal transformation, and k_B and T are the Boltzmann constant and temperature, respectively. Before applying equation (4) to predict the wurtzite to tetragonal transformation, it is noticed that the strain rate effect on mechanical behaviors results from the competition between two time scales. One is the external loading rate and the other is the frequency of thermal vibration of atoms in a material at a given temperature [46, 47]. Here, we particularly claim that $\dot{\varepsilon}_t$ and B in equation (4) represent the two opponents. The former has been determined by simulations in this study. The latter is around 10^{13} s^{-1} according to the upper limit of optical phonons of ZnO [50]. In a recent work, the same value was assumed to deal with the wurtzite to tetragonal phase transformation in ZnO NWs [20]. After B is ascertained, it is
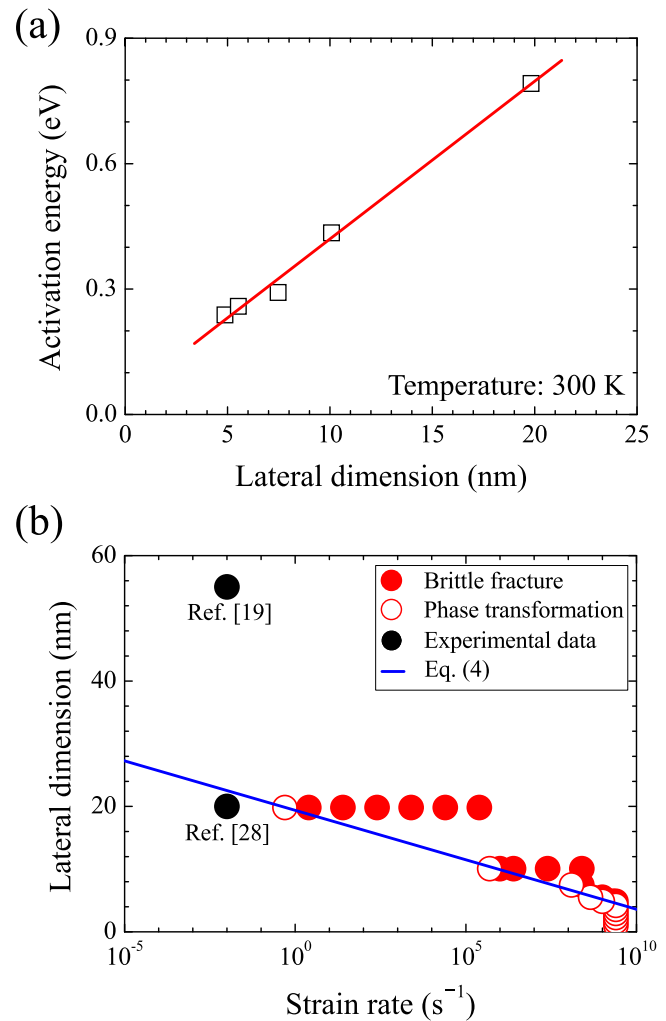

Figure 7. Size and strain rate dependent wurtzite-to-tetragonal phase transformation in ZnO NWs. (a) The activation energy grows proportionally as the lateral dimension of ZnO NWs increases. The line is a visual guide for the trend. (b) A summary of deformation behaviors of ZnO NWs with various lateral dimensions and strain rates. The line represents critical values below which phase transformation is allowed.

shown that the activation energy increases with the increase of the lateral dimension of NWs (see figure 7(a)). This is not surprising since the increase of lateral dimension cuts down the cohesive energy of a material due to reduction of surface region [26]. Thus, the energy barrier between wurtzite and tetragonal structures grows as the lateral dimension of NWs increases.

To compare the prediction of equation (4) with experimental results, let us review tensile protocols in the micro-electro-mechanical system based on the nanoscale testing technique [12, 19, 28]. According to this technique, an axial displacement is generated using a thermal actuator and loads are measured using a differential capacitive-based load sensor [34, 51]. The displacement–capacitance change relationship is calibrated by actuating an identical device with a series of stepwise increasing voltages [34]. The voltages are applied sequentially in several on–off cycles with each cycle lasting 20 s [34]. Here, we assume the strain rate is 10^{-2} s^{-1} given

that *in situ* tensile experiments were conducted under the quasi-static condition. By summarizing simulation results, experimental outcomes and prediction of equation (4) (see figure 7(b)), we find out that the case of 55 nm in [19] agrees well with the prediction of equation (4). However, tensile behavior of the 20 nm sample conflicts with prediction since the wurtzite to tetragonal phase transformation was not observed [28]. The absence of transformation could be caused by defects such as stacking faults and surface contamination, as indicated in sections 3.5 and 3.6.

4.2. Large dispersion of fracture strain of wurtzite ZnO NWs

Our study reveals that fracture strain of ZnO NWs depends on the wurtzite to tetragonal phase transformation. Fracture strains generated by wurtzite and tetragonal structures are around 10% and 20%, respectively. Here, we focus on the former by considering available experimental data of wurtzite structure. Based on our investigation, existence of defects leads to the large dispersion of fracture strain (hereafter refer to that of wurtzite NWs). Qualitatively different defects such as stacking faults and surface contamination could either weaken or enhance fracture strain.

Stacking faults are kind of defects which reduce fracture strain. As shown in figure 5, stacking faults yield fracture strains around 7.7% which are smaller than that, 9.9%, of a single crystalline wurtzite NW with a lateral dimension of 5.5 nm. The stacking fault generated fracture strain remains almost unchanged even as the parallel spacing between two adjacent stacking faults is up to 553 nm, which is equivalent to a dense of planar defect of 4.7×10^{-4} at%. A stacking fault breaks a periodic stacking regulation of wurtzite sequence and causes the lattice disregistry in its neighboring layers, leading to a natural source of cracks near these layers. A similar role of stacking faults caused weakening of fracture strain was confirmed in silicon carbide NWs [52]. Moreover, point defects such as vacancies are also reasons for resulting in reduction of fracture strain. The MD simulations have proven that vacancies can lower strain at the elastic limit of wurtzite ZnO NWs to 4%. This value falls in the middle of experimental tests, 2%–7% [21].

On the contrary, surface contamination is the reason to raise fracture strain. Nanomaterials are known to have considerable dangling bonds at their surface area due to the large surface-to-volume ratio [8, 9]. These bonds are highly active to react mutually or with an introducing impurity such as surface contamination. This inclination is utilized to improve deformability of a material and delay initiation of cracks at the surface area. This approach is referred to as the surface modification. Thus, facture strain of a NW reaches to 13.4% with the introduction of 0.7 at% surface impurity, as depicted in figure 6. The enhanced fracture strain, 13.4%, is well consistent with the upper bound, 12%–15%, experimentally discovered in wurtzite ZnO NWs [22]. Surface modification is also implemented to enlarge fracture strain of a lot of materials [53, 54].

5. Conclusions

We have shown that there is a wurtzite to tetragonal phase transformation in tensile behaviors of [0001]-oriented wurtzite ZnO NWs by means of MD simulations. Our systematic calculation reveals that the transformation depends significantly on the NW size and strain rate. By adopting the Arrhenius equation, these effects are elucidated through the competition between internally thermal motion of atoms and external loading rate. The former benefits the transformation whilst the latter dominates brittle fracture. Further, the large dispersion of fracture strain experimentally observed is attributed to the influence of defects. On one hand, stacking faults weaken fracture strain due to the lattice disregistry. On the other, surface contamination reinforces fracture strain via modification of dangling bonds on the surface of a NW. The finding provides a better understanding of how the wurtzite to tetragonal phase transformation occurs in a lot of II–VI, III–V and IV–IV ceramics. It has also highlighted the potential of tuning the mechanical behavior of nanostructures with defect engineering.

References

[1] Wang Z L and Song J H 2006 Piezoelectric nanogenerators based on zinc oxide nanowire arrays *Science* **312** 242–6

[2] Schrauben J H, Hayoun R, Valdez C N, Braten M, Fridley L and Mayer J M 2012 Titanium and zinc oxide nanoparticles are proton-coupled electron transfer agents *Science* **336** 1298–301

[3] You J *et al* 2016 Improved air stability of perovskite solar cells via solution-processed metal oxide transport layers *Nat. Nanotechnol.* **11** 75–81

[4] van Lare C, Lenzmann F, Verchuuren M A and Polman A 2015 Dielectric scattering patterns for efficient light trapping in thin-film solar cells *Nano Lett.* **15** 4846–52

[5] Wahab R, Kaushik N, Khan F, Kaushik N K, Choi E H, Musarrat J and Al-Khedhairy A A 2016 Self-styled ZnO nanostructures promotes the cancer cell damage and supresses the epithelial phenotype of glioblastoma *Sci. Rep.* **6** 19950

[6] Fang L, Liu B, Liu L, Li Y, Huang K and Zhang Q 2016 Direct electrochemistry of glucose oxidase immobilized on Au nanoparticles-functionalized 3D hierarchically ZnO nanostructures and its application to bioelectrochemical glucose sensor *Sensors Actuators* B **222** 1096–102

[7] Cheng G, Miao C, Qin Q, Li J, Xu F, Haftbaradaran H, Dickey E C, Gao H and Zhu Y 2015 Large anelasticity and associated energy dissipation in single-crystalline nanowires *Nat. Nanotechnol.* **10** 687–91

[8] Ma F and Xu K 2006 Surface induced electron redistribution: a mechanism for mechanical strengthening of Au nanowires *Scr. Mater.* **55** 951–4

[9] Liang W and Zhou M 2005 Pseudoelasticity of single crystalline Cu nanowires through reversible lattice reorientations *Trans. ASME, J. Eng. Mater. Technol.* **127** 423–33

[10] Kulkarni A J, Zhou M and Ke F J 2005 Orientation and size dependence of the elastic properties of zinc oxide nanobelts *Nanotechnology* **16** 2749–56

[11] Chen C Q, Shi Y, Zhang Y S, Zhu J and Yan Y J 2006 Size dependence of Young's modulus in ZnO nanowires *Phys. Rev. Lett.* **96** 075505

[12] Agrawal R, Peng B, Gdoutos E E and Espinosa H D 2008 Elasticity size effects in ZnO nanowires—a combined experimental-computational approach *Nano Lett.* **8** 3668–74

[13] Kulkarni A J, Zhou M, Sarasamak K and Limpijumnong S 2006 Novel phase transformation in ZnO nanowires under tensile loading *Phys. Rev. Lett.* **97** 105502

[14] Wang J, Kulkarni A J, Sarasamak K, Limpijumnong S, Ke F J and Zhou M 2007 Molecular dynamics and density functional studies of a body-centered-tetragonal polymorph Of ZnO *Phys. Rev.* B **76** 172103

[15] Fu B, Chen L, Xie Y, Feng J and Ye X 2015 Novel mechanical behaviors of wurtzite CdSe nanowires *J. Nanopart. Res.* **17** 354

[16] Wen B, Zhao J, Melnik R and Tian Y 2011 Body-centered tetragonal B_2N_2: a novel sp3 bonding boron nitride polymorph *Phys. Chem. Chem. Phys.* **13** 14565–70

[17] Jung K, Cho M and Zhou M 2014 Structure and thermomechanical behavior of bent GaN nanowires *Comp. Mater. Sci.* **81** 524–9

[18] Fujimoto Y, Koretsune T, Saito S, Miyake T and Oshiyama A 2008 A new crystalline phase of four-fold coordinated silicon and germanium *New J. Phys.* **10** 083001

[19] Agrawal R, Peng B and Espinosa H D 2009 Experimental-computational investigation of ZnO nanowires strength and fracture *Nano Lett.* **9** 4177–83

[20] Soldano G J, Zanotto F M and Mariscal M M 2015 Mechanical stability of zinc oxide nanowires under tensile loading: is wurtzite stable at the nanoscale? *RSC Adv.* **5** 43563–70

[21] He M R, Xiao P, Zhao J, Dai S, Ke F J and Zhu J 2011 Quantifying the defect-dominated size effect of fracture strain in single crystalline ZnO nanowires *J. Appl. Phys.* **109** 123504

[22] Desai A V and Haque M A 2007 Mechanical properties of ZnO nanowires *Sensors Actuators* A **134** 169–76

[23] Hoffmann S, Östlund F, Michler J, Fan H J, Zacharias M, Christiansen S H and Ballif C 2007 Fracture strength and Young's modulus of ZnO nanowires *Nanotechnology* **18** 205503

[24] Wang J, Kulkarni A J, Ke F J, Bai Y L and Zhou M 2008 Novel mechanical behavior of ZnO nanorods *Comput. Methods Appl. Mech. Eng.* **197** 3182–9

[25] He M R, Yu R and Zhu J 2012 Reversible wurtzite–tetragonal reconstruction in ZnO(100) surfaces *Angew. Chem., Int. Ed.* **51** 7744–7

[26] Ma F, Xu K W and Chu P K 2013 Surface-induced structural transformation in nanowires *Mater. Sci. Eng.* R **74** 173–209

[27] Wang F *et al* 2016 Nanometre-thick single-crystalline nanosheets grown at the water–air interface *Nat. Commun.* **7** 10444

[28] Xu F, Qin Q, Mishra A, Gu Y and Zhu Y 2010 Mechanical properties of ZnO nanowires under different loading modes *Nano Res.* **3** 271–80

[29] Agrawal R, Paci J T and Espinosa H D 2010 Large-scale density functional theory investigation of failure modes in ZnO nanowires *Nano Lett.* **10** 3432–8

[30] Ding Y, Zhang F and Wang Z L 2013 Deriving the three-dimensional structure of ZnO nanowires/nanobelts by scanning transmission electron microscope tomography *Nano Res.* **6** 253–62

[31] Ding Y and Wang Z L 2009 Structures of planar defects in ZnO nanobelts and nanowires *Micron* **40** 335–42

[32] Orsini A, Medaglia P G, Scarpellini D, Pizzoferrato R and Falconi C 2013 Towards high-performance, low-cost quartz sensors with high-density, well-separated, vertically aligned ZnO nanowires by low-temperature, seed-less, single-step, double-sided growth *Nanotechnology* **24** 355503

[33] Wang S, Fan Z, Koster R S, Fang C, van Huis M A, Yalcin A O, Tichelaar F D, Zandbergen H W and Vlugt T J H 2014 New *ab initio* based pair potential for accurate simulation of phase transitions in ZnO *J. Phys. Chem.* C **118** 11050–61

[34] Espinosa H D, Zhu Y and Moldovan N 2007 Design and operation of a MEMS-based material testing system for nanomechanical characterization *J. Microelectromech. Syst.* **16** 1219–31

[35] Song H Q, Shen J, Qian P and Chen N X 2014 Interfacial potential approach for Ag/ZnO (0001) interfaces *Chin. Phys.* B **23** 126801

[36] Wolf D, Keblinski P, Phillpot S R and Eggebrecht J 1999 Exact method for the simulation of Coulombic systems by spherically truncated, pairwise r–1 summation *J. Chem. Phys.* **110** 8254–82

[37] Melchionna S, Ciccotti G and Holian B L 1993 Hoover NPT dynamics for systems varying in shape and size *Mol. Phys.* **78** 533–44

[38] Smith W, Yong C W and Rodger P M 2002 DL_POLY: applications to molecular simulation *Mol. Simul.* **28** 385–471

[39] Nosé S 1984 A molecular dynamics method for simulations in the canonical ensemble *Mol. Phys.* **52** 255–68

[40] Hoover W G 1985 Canonical dynamics: equilibrium phase-space distribution *Phys. Rev.* A **31** 1695–7

[41] Binks D J and Grimes R W 1993 Incorporation of monovalent ions in ZnO and their influence on varistor degradation *J. Am. Ceram. Soc.* **76** 2370–2

[42] Pedone A, Malavasi G, Menziani M C, Cormack A N and Segre U 2006 A new self-consistent empirical interatomic potential model for oxides, silicates, and silica-based glasses *J. Phys. Chem.* B **110** 11780–95

[43] Raymand D, Duin A V, Baudin M and Hermansson K 2008 A reactive force field (ReaxFF) for zinc oxide *Surf. Sci.* **602** 1020–31

[44] Iwanaga H, Kunishige A and Takeuchi S 2000 Anisotropic thermal expansion in wurtzite-type crystals *J. Mater. Sci.* **35** 2451–4

[45] Serrano J, Manjón F J, Romero A H, Ivanov A, Cardona M, Lauck R, Bosak A and Krisch M 2010 Phonon dispersion relations of zinc oxide: inelastic neutron scattering and *ab initio* calculations *Phys. Rev.* B **81** 174304

[46] Xiao P, Wang J, Yang R, Ke F J and Bai Y L 2015 Transition of mechanisms underlying the rate effects and its significance *Comput. Mater. Sci.* **98** 70–5

[47] Xiao P, Wang J, Yang R, Ke F J, Xia M F and Bai Y L 2013 Rate effect and coupled evolution of atomic motions and potential landscapes *Acta Mech. Sin.* **29** 676–81

[48] Humphrey W, Dalke A and Schulten K 1996 VMD: visual molecular dynamics *J. Mol. Graph.* **14** 33–8

[49] Lindefelt U, Iwata H, Öberg S and Briddon P R 2003 Stacking faults in 3C–, 4H–, and 6H–SiC polytypes investigated by an *ab initio* supercell method *Phys. Rev.* B **67** 155204

[50] Wang Z, Wang F, Wang L, Jia Y and Sun Q 2013 First-principles study of negative thermal expansion in zinc oxide *J. Appl. Phys.* **114** 063508

[51] Wang W, Li S, Zhang H and Lu Y 2015 Recent developments in testing techniques for elastic mechanical properties of 1D nanomaterials *Recent Patents Nanotechnol.* **9** 33–42

[52] Cheng G, Chang T H, Qin Q, Huang H and Zhu Y 2014 Mechanical properties of silicon carbide nanowires: effect of size-dependent defect density *Nano Lett.* **14** 754–8

[53] Zhang L J, Yang D L, Qiu F, Wang J G and Jiang Q C 2015 Effects of reinforcement surface modification on the microstructures and tensile properties of SiCp/Al2014 composites *Mater. Sci. Eng.* A **624** 102–9

[54] Shikinaka K, Abe A and Shigehara K 2015 Nanohybrid film consisted of hydrophobized imogolite and various aliphatic polyesters *Polymer* **68** 279–83